Substrate Roughness Influence on the Order of Nanografted Self-Assembled Monolayers

Denis Scaini[1,2], Fabio Biscarini[3,4], Loredana Casalis[2] and Cristiano Albonetti[5]*

1. University of Basque Country (UPV/EHU) Avenida Miguel de Unamuno 3, 01006, Vitoria-Gasteiz, Spain; IKERBASQUE, Basque Foundation for Science, 48009, Bilbao, Spain

2. NanoInnovation Lab, Elettra Sincrotrone Trieste S.C.p.A., 34149 Trieste, Italy

3. Center for Translational Neurophysiology - Istituto Italiano di Tecnologia, Via Fossato di Mortara 17-19, 44100 Ferrara, Italy

4. Dipartimento di Scienze della Vita - Università di Modena e Reggio Emilia, Via Campi 103, 41125 Modena, Italy

5. Consiglio Nazionale delle Ricerche - Istituto per lo Studio dei Materiali Nanostrutturati (CNR-ISMN), Via P. Gobetti 101, 40129 Bologna, Italy

Abstract

Adjacent patches of alkanethiol molecules whose chain lengths range from 11 to 15 carbon atoms are fabricated by nanografting within a Self-Assembled Monolayer matrix. Atomic Force Microscopy and Electrostatic Force Microscopy are employed to investigate their structural and electronic properties, highlighting the key role of the substrate roughness. In particular, the topographic phase signal allows to establish an odd-even dependence of the local stiffness versus the alkyl chain length, while the electrostatic force signal provides evidence that the conformational order versus the alkyl chain length follows an asymmetric parabolic trend induced by the substrate roughness.

Introduction

In the vast literature on alkanethiol Self-Assembled Monolayers (SAMs) [1], most of the studies on their structural and electronic properties were carried out employing techniques that operate on a large area, i.e. the information is averaged on a few mm^2, like X-ray Photoelectron Spectroscopy [2] or Kelvin Probe [3]. On smaller areas, i.e. hundreds of nm^2 or below, Scanning Tunneling Microscopy investigations [4] were carried out to obtain complementary information that is difficult to extend to larger areas. Bimodal Atomic Force Microscopy (AFM) [5], Kelvin Probe Force Microscopy [6–8] and Electrostatic Force Microscopy (EFM) [9] have successfully up scaled the information on structural and electronic properties from nm to micrometric scale. In those works, SAMs of diverse alkyl chain length were individually prepared. In this study we exploit nanografting, a lithographic approach based on AFM [10,11], to fabricate micrometric patches of alkanethiol SAMs characterized by alkyl chains of increasing lengths (from 10 to 15 carbon atoms). Then, AFM [12] and EFM [13] phase imaging are employed to investigate their structural and electronic properties, and to establish their dependence on the substrate roughness. The validity of this differential comparison of molecular properties was already demonstrated by measuring the tunneling decay constant of alkanethiols as a function of their length [14].

Materials and Methods

Materials. The substrates are prepared by evaporating Au (99.99% pure, from Metalli Preziosi S.p.a., Milan, Italy) on muscovite mica (Goodfellow Cambridge Limited, Huntingdon, England). SAMs solutions are obtained dissolving alkanethiols in ethanol (99.8%, from Fluka and Sigma Aldrich) at a final concentration of 100 mM. Five alkanethiol molecules with increasing alkyl chain length have been chosen for this study (all from Sigma Aldrich): 1-decanethiol ($CH_3(CH_2)_9SH$), 1-undecanethiol ($CH_3(CH_2)_{10}SH$), 1-dodecanethiol ($CH_3(CH_2)_{11}SH$), 1-tetradecanethiol ($CH_3(CH_2)_{13}SH$) and 1-

pentadecanethiol (CH$_3$(CH$_2$)$_{14}$SH). The chain length is indicated with Cn, where n stands for the number of carbon atoms (e.g., C10 indicates 1-decanethiol). Thus, n ranges from 10 to 15 here.

Preparation of Au Substrates and SAM Matrices. Two kinds of Template Stripped Gold (TSG) ultra-flat substrates are prepared for this work: annealed (SUB1) and not annealed (SUB2). In both cases, an Au layer (100 nm thick) is deposited at moderate deposition rate (≈ 0.1 nm·s^{-1}), using an electron beam evaporator in vacuum (10^{-6} mbar), on a freshly cleaved piece of mica. SUB1 films are immediately flame annealed with a reducing hydrogen torch flame [15], and subsequently quenched in a stream of nitrogen. SUB2 substrates are prepared following the Template Stripped Gold (TSG) procedure, as described by Gupta [16]. In short, samples are glued from the Au side to small pieces of fused silica (about 5 mm × 5 mm in side size, 0.5 mm thick) with a drop of SU8-100 (Kayaku Advanced Materials, MA, USA). Then the polymer is cured (20 minutes under a 70 µW·cm^{-2}, 462 nm, UV lamp and baked at least 3 hours at 95°C). The ultra-flat Au surface is cleaved from the Au–mica interface by using a razor blade. Freshly annealed and peeled samples are immediately soaked in a freshly prepared 100 mM solution of C10 alkanethiol in ethanol to obtain a SAM hosting carpet acting as a molecular reference. After an incubation time of 24 h, samples are rinsed with pure ethanol and dried in a gentle blow of nitrogen and mounted in the liquid cell of the nanolithographic AFM. The C10 SAM formed on both substrates represents the matrix for the nanografting process and a barrier preventing the lateral diffusion of patch-immobilized thiolated molecules. From now on, it will be termed C10 matrix. In SUB1, Au annealing gives rise to grains composed of flat terraces (typical dimensions of about 1.0 µm) with an average roughness of ≈1 Å [15] (see Fig. 1a). In SUB2, Au grows in contact with the mica surface reproducing its morphology and flatness in the form of randomly oriented grain edges resulting in a macroscopically flat surface with a roughness of ≈3 Å [17] (see Fig. 1b).

Fabrication of Alkanethiol Patches with Nanografting. Nanografting has been performed with a Solver PRO AFM microscope (NT-MDT, Zelenograd, Moscow, RU) in an open liquid cell using silicon rectangular cantilevers (MikroMash NSC36/noAl, spring constant $k \approx 0.6$ nN·nm^{-1}). Micrometric and sub-micrometric patches embedded in the matrix have been fabricated using the Xu procedure [18]. The matrix has been imaged first at a very low force (≈ 0.5 nN) in an ethanol solution of alkanethiol (grafting concentration $c = 50$ mM). Then, the C10 molecules have been shaved upon scanning a small portion of the surface at high force (≈ 50 nN) and high scan rate (1 μm·s^{-1}). A single raster scan is enough to expose the underlying Au film. Shaved off C10 molecules disperse in the solution where the target alkanethiol molecules are present at high concentration, thus immediately leading to self-assembly on the freshly exposed Au. The result is a patch of the target alkanethiol embedded within the C10 matrix. Reproducible, well-ordered and densely packed patches are fabricated keeping the shaving force, the scan rate, and the alkanethiol concentration constant during all the experiments [14]. In particular, a scan rate of 1 μm·s^{-1} enables to grow patches composed of large alkanethiol domains and with a molecular packing comparable to SAMs obtained by classical wet assembly [19]. Two kinds of nanografted samples have been fabricated: sub-micrometric patches of about 0.75×0.75 μm^2 on the SUB1 surface (C11-C12-C14-C15, Sample1) and micrometric patches (2×2 μm^2) on the SUB2 substrate (C14-C15, Sample2). Based on the results obtained using Sample1, Sample2 has been specifically prepared only with C14 and C15 in order to test the effects of Au substrate roughness. The lateral dimensions of the patches for both samples are large enough to yield a molecular packing and, consequently, a Young's modulus comparable to those of solution-assembled SAMs [20]. This evidence supports once again the general scalability of the nanografting process [21].

AFM Phase Imaging. Intermittent Contact Mode (ICM) is an AFM technique in which the amplitude modulation allows to evaluate the morphology and the phase the local stiffness [22]. The averaged tip–sample force $\langle F_{ts} \rangle$ is relatively low for a high amplitude set-point A_{SP} (in nm), correspondent to a small

reduction of the free oscillation amplitude of the cantilever A_0 (in nm, attractive regime), while it becomes relatively high for a low A_{SP}, i.e. in a high decrease of A_0 (repulsive regime). $\langle F_{ts} \rangle$ can be calculated using the relationship reported by García [23] with the cantilever elastic constant k (in N·m^{-1}) calibrated with the Sader method [24]:

$$\langle F_{ts} \rangle = \frac{F_0}{2} \sqrt{1 - \left(\frac{A_{SP}}{A_o} \right)^2} \tag{1}$$

where the driving force F_0 (in nN) is $A_0 \cdot k$. The ICM measurements are performed with silicon cantilevers coated with Pt (NSC36/Pt, MikroMash, Sofia, Bulgaria). The topographic images are collected in the repulsive regime employing two different cantilevers exerting an average force $\langle F_{ts} \rangle$ of ≈ 6.1 and 11.3 nN.

Simultaneously to the topographic image, the phase image is recorded on the whole area. Away from the surface, the phase θ (in rad) of the free cantilever oscillations is equal to $\pi/2$ with respect to the sinusoidal driving signal[1]. When the tip interacts with the surface, its energy is partially dissipated and a phase lag $\Delta\theta$ occurs [25]. The phase θ is then $\pi/2 + \Delta\theta$, with $\theta > \pi/2$ in the attractive regime and $\theta < \pi/2$ in the repulsive regime, as reported by Cleveland [26]. Thus, $\Delta\theta$ is positive when the tip is in the repulsive regime and negative in the attractive one. In the repulsive regime, the tip indents the surface and the overall derivative forces σ exerted by the tip on the sample can be approximated to the local time-averaged sample stiffness $\langle S \rangle$, if $\sigma << k$ [22]. This approximation holds true in our case, hence the phase lag $\Delta\theta$ can be related to the local stiffness $\langle S \rangle$ through the relationship:

$$\langle S \rangle = \frac{k}{Q} \Delta\theta \tag{2}$$

---

[1] Two different notations are used to distinguishing the mechanical phase, θ, from the electrical one, φ.

where Q is the cantilever quality factor. As shown in Eq. 2, phase imaging provides a map of the stiffness variations of the sample surface (i.e. a stiffer region presents a larger $\Delta\theta$). As described in the phase imaging theory [27], $\langle S \rangle$ can be correlated to the effective Young modulus E^* and the time-averaged value of the tip contact area $\langle A \rangle$:

$$\langle S \rangle \propto \sqrt{\langle A \rangle} \cdot E^* \Rightarrow \Delta\theta \propto \frac{Q}{k} \sqrt{\langle A \rangle} \cdot E^* \tag{3}$$

Eq. 3 shows that $\langle S \rangle$ is proportional to E^*, that is dominated by the modulus of the sample when the tip is much stiffer than the sample. SAMs with a length from 5 to 18 exhibit E_{SAM} ranging from ≈ 0.1 to ≈ 1 GPa, respectively [28]. In our case, the tip is coated with a Pt film ≈ 20 nm thick with $E_{Pt} \approx 160$ GPa [29]. Thus, we have $E_{Pt} \gg E_{SAM}$ and phase imaging should distinguish patches with different Young's moduli. However, the stiffness is also proportional to $\langle A \rangle^{\frac{1}{2}}$, and a softer material could have a larger contact area $\langle A \rangle$ thus yielding an enhanced phase contrast. This is the case of phase imaging on polymers [22], where $\langle S \rangle$ is larger on a surface region with smaller Young's modulus if $\langle A \rangle$ dominates $\langle S \rangle$.

EFM Phase Imaging. In Phase-mode EFM (EFM-Phase), electrostatic imaging can be performed using a dual pass system: in the first pass, the topography is recorded in standard amplitude modulation ICM; in the second pass the tip is lifted up to a fixed height $H = 50$ nm above the surface and moved along the previously recorded topographic profile while applying a DC bias voltage to the tip (V_{tip}) with respect to the grounded substrate [13]. The phase signal depends exclusively upon the electrostatic interaction between the oscillating tip and the surface held at a constant separation. For a null electrostatic interaction, φ_i, is equal to $\pi/2$. A Smena AFM microscope (NT-MDT, Zelenograd, Moscow, RU) and silicon cantilevers coated with Pt are employed for these measurements. The samples are electrostatically

characterized by measuring $\varphi_i(V)$ for $-2.5 \leq V_{tip} \leq 2.5$ V, a voltage range leading to the linear dependence of φ_i vs. V [13].

Results

Mechanical response. Due to the limited difference in length between the grafted and the hosting molecules, it is difficult to distinguish the patches from the color contrast in the topographic images of the two samples (Fig. 2a-c), while molecular patches are easily distinguishable in term of contrast in the phase images (Fig. 2b-d). The analysis of topographic profiles across a patch is useful by the fact the step height of the top of the patch with respect to the reference matrix is indicative of the molecular packing [30]. From the cross-section of the C15 patch a step height in agreement with the literature is obtained [3]. However, Sample1 shows a step height of ≈ 0.3 nm (see the inset of Fig. 2a) whereas in Sample2 it increases to ≈ 0.9 nm (see the inset of Fig. 2c). This difference can be ascribed to either the imaging force $\langle F_{ts} \rangle$, doubled for Sample2, or to the Young's modulus that increases at increasing alkanethiol lengths or both. By using the force-indentation curves reported in Ref. [28], the difference between the indentation of C10 and C15 SAMs is ≈ 0.4 nm, close to the step height of Sample1.

In the phase image of Sample1, patches show an increasingly brighter contrast for increasing alkyl chain length (see Fig. 2b, from C12 to C15), except for the C11 patch that has a phase contrast slightly different to the C10 matrix (only 0.009 rad). By analysing the phase contrast on the base of Eq. 3, $\Delta\theta_{C10} < \Delta\theta_{Cn}$ for all n because of the Young modulus increases for increasing alkyl chain length [28]. Eq.3 includes also the square-root of $\langle A \rangle$ that works at the opposite of E^*. Indeed, a softer SAM leads to a larger contact area $\langle A \rangle$ and thus $\Delta\theta$ decreases for alkyl chain length. The combination of E^* and $\langle A \rangle$ can explain the little phase contrast observed in the C11 patch: a distinct transition of SAMs from a liquid-like to a crystalline phase occurs at C11 [31] together with a transition from disordered to ordered films was observed in the range from C10 to C12 [32], so $E^*_{C10} < E^*_{C11}$ but $\langle A \rangle_{C10} > \langle A \rangle_{C11}$ hence $\Delta\theta_{C10} \lesssim$

$\Delta\theta_{C11}$. As visible in Figure 2a, the C11 patch is the only patch formed on Au monoatomic steps; possibly, this might be responsible for additional molecular disorder (see Supplementary Materials).

For Sample2 (see Fig. 2d), the phase contrast increases as well with increasing the alkyl chain length, but the phase contrast of the patches is less pronounced and homogeneous compared to Sample1. These observations could be due, respectively, to: (i) similar Young moduli for C14 and C15 or, (ii) a morphological disorder induced by the roughness of SUB1 and enhanced by the higher imaging force $\langle F_{ts} \rangle$. The average stiffness $\langle S \rangle$ calculated from Eq.2 encompasses these observations. As shown in Fig. 3, $\langle S \rangle$ is proportional to E^* for both samples and increases for increasing chain length [28]. The linear regression of Sample1 (dashed green line) points out an odd-even effect of $\langle S \rangle$ that may be correlated to what is reported in the literature [33]. The odd-even effect is hindered in Sample2: a larger imaging force $\langle F_{ts} \rangle$ may cause a greater $\langle A \rangle$ and thus a higher $\langle S \rangle$, which is consistent with the phase contrast observed on the patches in Fig. 2d that are less homogeneous thus with larger $\langle S \rangle$ error bars. Thus, a packing disorder of the patches induced by the roughness of SUB2 seems to be responsible for this behaviour because the disorder increases the SAM compressibility making $\langle S \rangle$ almost constant. This increased compressibility hints a possible explanation on the larger step height measured on Sample2.

Electrostatic response. The electrostatic contrast of the C10 matrix for Sample1 and Sample2 is firstly investigated. For Sample1, the phase curve φ_i versus V_{tip} can be fitted with a parabola (sand color solid line in Fig. 4a) with the following formula:

$$\varphi_i = \frac{\pi}{2} + \frac{Q \cdot (V_{tip} - V_0)^2}{2 \cdot k} \frac{d^2 C}{dz^2} \Rightarrow \varphi_i = \left(\frac{\pi}{2} - a\right) + b \cdot (V_{tip} - c)^2 \tag{4}$$

where C is the tip-sample capacitance, z is the tip-sample distance, a (in rad) is the vertical offset, b (in V^{-2}) is the parabola stretching and c (in V) is the horizontal translation V_0 at $V_{tip} = 0$ embodying static

charges, surface polarization and work function difference between the tip and the sample, also defined Contact Potential Difference, CPD (see Supplementary Materials for the full demonstration of Eq. 4).

The term b depends on the cantilever properties, through Q/k and the tip–sample capacitance d^2C/dz^2 that represents the sensitivity of the EFM-phase measurement for which a higher b produces a larger φ_i. For Sample1, b is $(1.76 \pm 0.05)\cdot10^{-2}$ V^{-2} and $d^2C/dz^2 = (3.7 \pm 0.1)\cdot10^{-4}$ F·m^{-2} with $Q/k \approx 94$, values comparable to the highest stretched parabola obtained on Au samples with Pt tips [13].

The CPD, i.e. $c = V_0 = (0.08 \pm 0.02)$ V, is related to the general form of the work function Φ for a metal [34]:

$$\Phi = \Phi_{bulk} + V_D \tag{5}$$

where Φ_{bulk} is the bulk work function and V_D is the potential shift due to the total dipole produced by the sum of the SAM dipoles with a potential shift of $V_{D\text{-}SAM}$, and the dipole due to the adsorbed molecules from air, with $V_{D\text{-}ADS}$. Considering the work function of the tip Φ_{tip} as the reference electrode, the CPD is equal to:

$$V_0 = \frac{\Phi_{tip} - \Phi_{sample}}{-e} = \frac{\Phi_{tip,bulk} + V_{D-ADS} - \Phi_{sample,bulk} - V_{D-ADS} - V_{D-SAM}}{-e}$$
$$= \frac{\Delta\Phi_{bulk} - V_{D-SAM}}{-e} \tag{6}$$

where $V_{D\text{-}ADS}$ is assumed equal for tip and sample metals. The polycrystalline Pt tip has $\Phi_{Pt,bulk} = 5.65$ eV, while the Au(111) surface of SUB1 has $\Phi_{Au\text{-}bulk} = 5.31$ eV [35]. Therefore, $\Delta\Phi_{bulk}$ is 0.34 eV. The positive sign of V_0 for the SAM/Au surface is opposite with respect to the negative one obtained on bare polycrystalline Au [13]. This is consistent with the presence of a dipole sheet on the Au surface [36] that modulates the Au work function shifting the vacuum energy level [37]. From Eq. 6, the potential shift

induced by the C10 matrix is $V_{D\text{-}OL} = eV_0 + \Delta\Phi_{bulk} \approx (0.42 \pm 0.02)$ eV. Then, the Au work function increases in agreement to both Eq. 5 and the literature (see Supplementary Materials of Ref. [38]).

For Sample2, the phase curve φ_i versus V_{tip} is asymmetric (see Fig. 4b) and data fitting is possible with a linear combination of two parabolas in two consecutive V_{tip} ranges, i.e. [-1.5; 1] and [1; 2.5] V. Asymmetric parabolic branches can be fitted with two parabolas (purple solid line in Fig. 4b) characterized by different stretching b: one relatively small (pink dashed line), the other relatively high (green dashed line). The fitting curve has a geometric continuity in $V_{tip} = 1$ V where the two parabolas merge together within the absolute error of φ_i (1 V) (see the inset in Fig. 4b).

The horizontal translation of the fitting curve, i.e. $c = (0.84 \pm 0.05)$ V, is determined by the right parabolic branch. The polycrystalline surface of SUB2 has $\Phi_{Au\text{-}bulk} = 5.1$ eV [35]. Therefore, $\Delta\Phi_{bulk}$ is 0.55 eV. From Eq. 6, the potential shift induced by the C10 SAM for Sample2 is $V_{D\text{-}SAM} \approx (1.39 \pm 0.05)$ eV, that is higher than the one calculated for Sample1. The parabola stretching b for the left branch is $(0.75 \pm 0.08) \cdot 10^{-2}$ V^{-2}, correspondent to a $d^2C/dz^2 = (1.5 \pm 0.2) \cdot 10^{-4}$ F·m^{-2} with $Q/k \approx 97$, values comparable to the lowest stretched parabola obtained on polycrystalline Au imaged by Co tips [13]. In the right parabolic branch, the phase sensitivity is much larger than the left one with $b = (2.37 \pm 0.14) \cdot 10^{-2}$ V^{-2} and then $d^2C/dz^2 = (4.9 \pm 0.3) \cdot 10^{-4}$ F·m^{-2}. Like for the mechanical properties, the morphological disorder induced by the roughness of SUB2 seems to affect the electrical properties of the C10 matrix.

The alkanethiol patches can be analysed on the basis of the interpretative framework prepared for the C10 matrix. The electrostatic contrast increases for increasing alkyl chain length in both samples, except for C11 where the electrostatic contrast is equal to the C10 matrix (as an example, Fig. 5 shows EFM-phase images for $V_{tip} = -1.5$ V; movies with full V_{tip} ranges are available in Multimedia materials). Such an increased contrast corresponds to an increase of φ_i [39], which is due to the increase of the molecular polarizability with the chain length [3].

	Cn	a	B	c	d^2C/dz^2	$V_{D\text{-}SAM}$
		$\times 10^{-2}$ rad	$\times 10^{-2}$ V^{-2}	V	$\times 10^{-4}$ F·m^{-2}	eV
Sample1	10	0.8	1.76 ± 0.05	0.08 ± 0.02	3.7 ± 0.1	0.42 ± 0.02
	11	0.8	1.76 ± 0.05	0.08 ± 0.02	3.7 ± 0.1	0.42 ± 0.02
	12	0.9	1.75 ± 0.05	0.15 ± 0.02	3.7 ± 0.1	0.49 ± 0.02
	14	0.6	1.77 ± 0.04	0.51 ± 0.02	3.79 ± 0.09	0.85 ± 0.02
	15	0.8	1.70 ± 0.05	0.67 ± 0.02	3.62 ± 0.11	1.01 ± 0.02
Sample2	10	1	0.75 ± 0.08 (L) 2.37 ± 0.14 (R)	0.84 ± 0.05	1.5 ± 0.2 (L) 4.9 ± 0.3 (R)	1.39 ± 0.05
	14	0.9	0.64 ± 0.07 (L) 2.27 ± 0.18 (R)	0.98 ± 0.05	1.3 ± 0.1 (L) 4.7 ± 0.4 (R)	1.53 ± 0.05
	15	0.9	0.73 ± 0.09 (L) 2.24 ± 0.20 (R)	0.99 ± 0.06	1.5 ± 0.2 (L) 4.6 ± 0.4 (R)	1.54 ± 0.06

Table 1: Parameters extracted or calculated from the parabolic fitting of data for Sample1 and Sample2. For both samples, a is negligible.

As shown in Fig. 6, the phase curves of the patches shift progressively towards more positive values of V_{tip} for increasing Cn, in agreement with the literature [3]. As reported in Table 1, Sample1 exhibits a large shift of $V_{D\text{-}SAM}$ for C14 and C15 vs. C10, whereas this shift is little for Sample2. The term b is constant to $(1.75 \pm 0.05) \cdot 10^{-2}$ V^{-2} for Sample1 and to $(0.71 \pm 0.08) \cdot 10^{-2}$ and $(2.29 \pm 0.17) \cdot 10^{-2}$ V^{-2} for the left and right branch of Sample2, respectively. Accordingly, d^2C/dz^2 values are $(3.7 \pm 0.1) \cdot 10^{-4}$ F·m^{-2} for Sample1 and (1.5 ± 0.2), $(4.7 \pm 0.4) \cdot 10^{-4}$ F·m^{-2} for Sample2.

At a zeroth-order approximation, the tip-sample capacitance C depends on the distance z between the tip and the Au/SAM interface, which is assumed as the reference interface. Such distance is $H + t$ where H is referred to the sample surface and t is the SAM thickness. The capacitance C is the series of

the tip, C_{tip}, and the SAM, C_{SAM}, capacitances. As proved in the Supplementary Materials, C_{tip} referred the bare Au surface at a distance H is always larger than C at a distance z, which is why SAM reduces the system capacitance. The capacitance per unit area (F·m^{-2}) of the SAM layer is expressed by $C_{SAM} = \varepsilon_0 \cdot \varepsilon_{SAM} \cdot t^{-1}$ where ε_0 is the vacuum permittivity and ε_{SAM} is the relative permittivity of the SAM, fixed to (2.7 ± 0.3) [40]. Consequently, the larger is t the smaller is C_{SAM}. The second derivative of C is $d^2C/dz^2 \sim \delta^2C/\delta t^2 = 2\varepsilon_0 \cdot \varepsilon_{SAM} \cdot (\varepsilon_0 \cdot \varepsilon_{SAM} \cdot C_{tip}^{-1} + t)^{-3}$, therefore d^2C/dz^2 has to decrease for increasing alkyl chain length (see Supplementary Materials). As shown in Table 1, this effect is clear in the right branch of Sample2, but it is hindered by experimental errors, probably due to a resolution loss caused by the relatively high H [13]. On the other hand, d^2C/dz^2 is clearly different for Sample1 and Sample2 where, apparently, SAMs are thinner in Sample1 versus Sample2 for the left branch, while they appear thicker in the right one.

In both samples, the potential shift V_0 induced by SAMs increases progressively for increasing alkyl chain length. As shown in Fig. 7, V_0 shows two linear fitting in Cn ranges from C10 to C12 and from C12 to C15 for Sample1. The linear slope, i.e. the potential shift per methylene units (-CH$_2$-), is (0.035 ± 0.020) V = (35 ± 20) mV in the first range, a value comparable with the literature [2]. In the second Cn range, V_0 is (174 ± 5) mV, almost five times larger and suggesting an improved order of the patches with longer alkyl chain length on SUB1 [41]. *Vice versa*, the relative disorder induced by SUB2 in Sample2 back again the slope to (32 ± 4) mV, which agrees to the result obtained in the range from C10 to C12 of Sample1.

Discussion

The C10 matrix and the nanografted patches may be considered a two dimensional dipole sheet [3]. Its orientation can inferred from the positive shift of CPD with respect to bare Au [13] that, in molecular terms, implies an effective dipole R$^+$-S$^-$, with R=C$_n$H$_{2n+1}$, larger than the Au$^+$-S$^-$ dipole [3].

The R$^+$-S$^-$ dipole measured by EFM has a direction normal to the surface and a magnitude on dependent on the alkyl chain length and its tilt angle Ω [42]. Thus, Ω introduces a structural effect on the modulation of $\Phi_{Au\text{-}bulk}$ by SAMs (also dependent on molecular (dis)order [38,43]), while the aforementioned molecular scheme explains why $\Phi_{Au\text{-}bulk}$ is modulated by SAMs [44]. The potential shift $V_{D\text{-}SAM}$ of the vacuum energy level per unit area (V·m^{-2}) induced by the dipoles sheet is [45]:

$$V_{D-SAM} = \frac{N_{mol} \cdot \mu \cdot \cos\Omega}{\varepsilon_{SAM}\varepsilon_0} \tag{7}$$

where N_{mol} (in molecules/m^2) is the alkanethiol surface density and μ is the magnitude of the total dipole moment (in C·m or Debye D).

As reported in previous studies [2], μ has an average value of ≈ 2.45 D and is rather insensitive to the number of methylene units (-CH$_2$-), changing by ≈ 0.2 D as the chain grows from C3 to C18. This modest change cannot be responsible for the large slope per CH$_2$ observed in the range from C12 to C15, suggesting that a structural effect of the dipole sheet affects $V_{D\text{-}SAM}$ (see Supplementary Materials for a rough calculation of Ω).

As aforementioned, the range from C10 to C12 marks a transition region [32], where SAMs shift from a lesser conformational order (liquid-like, disorder phase, lower N_{mol} and higher average tilt angle Ω) to a higher one (crystalline-like, ordered phase, higher N_{mol} and lower average tilt angle Ω) [46]. At or above C14, the alkanethiols are well-ordered/highly packed and form rigid, crystalline SAMs where the alkyl chains exhibit all-trans conformations [47]. At the opposite, the slope measured on SUB2 in the range from C10 to C15 is comparable to one measured on SUB1 in the range from C10 to C12, suggesting that the increased roughness of SUB2 augments intentionally the disorder phase of the C14 and C15 patches making them comparable to the intrinsic disordered phase of SAMs in the range from C10 to C12.

Additional evidence of an order/disorder transition comes from the symmetry loss of the EFM-phase parabolas in Sample2 (see Fig. 6). Such deviated parabolas lose symmetry under negative voltages where a linear combination of parabolas is necessary to fit the raw data (see Fig. 6b). These observations are peculiar and similar to the one observed in van der Waals heterostructures [48]. The asymmetric parabolic behavior suggests an electric field screening in Sample2, as confirmed also by the capacitance C and its double derivatives d^2C/dz^2 (see Table 1), that changes slightly in the left and right branches with a higher and lower parabolic stretching, respectively. A conformational disorder of the alkanethiols induced by the SUB2 roughness might be responsible to this asymmetry (see the sketch in Fig. 8): a higher molecular disorder means a lower molecular surface density N_{mol} and a higher tilt angle Ω, leaving exposed the negative charges at the Au/SAM interface to the negative charges of the EFM tip. Such tip charges are therefore screened by the negative charges of the sample, causing a lower electric force and thus lower φ_i values. The opposite occurs when the tip is positively biased, with an increase of both the electric force and φ_i values. This order/disorder effect reminds to the one induced by the curvature radius on the SAM shell of Au nanoparticles [49].

Conclusions

The structural and electronic properties of alkanethiol SAMs with increasing alkane chain length from C10 to C15 have been herein investigated. The use of the nanografting technique, by forming patches of different alkane chain length in the same scanned area, enabled a genuine differential comparison of molecular properties. AFM phase imaging has been able to highlight the odd-even effect for the stiffness vs. chain length, while EFM phase imaging has provided deeper details of the conformational alkanethiol order. Their combination has allowed to identify the role of the substrate roughness in the packing order of the SAMs patches.

Credit authorship contribution statement

Denis Scaini: Investigation, Validation, Methodology, Writing – review & editing; **Loredana Casalis:** Conceptualization, Supervision, Funding, Writing – review & editing; **Fabio Biscarini:** Conceptualization, Supervision, Funding, Writing – review & editing; **Cristiano Albonetti:** Conceptualization, Investigation, Validation, Methodology, Data analysis, Calculations, Writing original draft.

Declaration of Competing Interest

The authors declare that they have no known competing financial interest or personal relationship that could have appeared to influence the work reported in this paper.

Acknowledgment

Appendix A. Supplementary material

Supplementary data to this article can be found online at:

References

[1]   J.C. Love, L. a Estroff, J.K. Kriebel, R.G. Nuzzo, G.M. Whitesides, Self-assembled monolayers of thiolates on metals as a form of nanotechnology., Chem. Rev. 105 (2005) 1103–1169.

[2]   D.M. Alloway, M. Hofmann, D.L. Smith, N.E. Gruhn, A.L. Graham, R. Colorado, V.H. Wysocki, T.R. Lee, P.A. Lee, N.R. Armstrong, Interface Dipoles Arising from Self-Assembled Monolayers on Gold: UV−Photoemission Studies of Alkanethiols and Partially Fluorinated Alkanethiols, J. Phys. Chem. B. 107 (2003) 11690–11699. https://doi.org/10.1021/jp034665+.

[3]   S.D. Evans, A. Ulman, Surface potential studies of alkyl-thiol monolayers adsorbed on gold,

Chem. Phys. Lett. 170 (1990) 462–466. https://doi.org/10.1016/S0009-2614(90)87085-6.

[4]   Q. Guo, F. Li, Self-assembled alkanethiol monolayers on gold surfaces: resolving the complex structure at the interface by STM, Phys. Chem. Chem. Phys. 16 (2014) 19074–19090. https://doi.org/10.1039/C4CP00596A.

[5]   C. Albonetti, S. Casalini, F. Borgatti, L. Floreano, F. Biscarini, Morphological and mechanical properties of alkanethiol self-assembled monolayers investigated via bimodal atomic force microscopy, Chem. Commun. (2011). https://doi.org/10.1039/c1cc12567b.

[6]   J. Lü, E. Delamarche, L. Eng, R. Bennewitz, E. Meyer, H.-J. Güntherodt, Kelvin Probe Force Microscopy on Surfaces: Investigation of the Surface Potential of Self-Assembled Monolayers on Gold, Langmuir. 15 (1999) 8184–8188. https://doi.org/10.1021/la9904861.

[7]   J. Lü, L. Eng, R. Bennewitz, E. Meyer, H.-J. Güntherodt, E. Delamarche, L. Scandella, Surface potential studies of self-assembling monolayers using Kelvin probe force microscopy, Surf. Interface Anal. 27 (1999) 368–373. https://doi.org/https://doi.org/10.1002/(SICI)1096-9918(199905/06)27:5/6<368::AID-SIA530>3.0.CO;2-W.

[8]   B. Moores, J. Simons, S. Xu, Z. Leonenko, AFM-assisted fabrication of thiol SAM pattern with alternating quantified surface potential, Nanoscale Res. Lett. 6 (2011) 185. https://doi.org/10.1186/1556-276X-6-185.

[9]   S. Howell, D. Kuila, B. Kasibhatla, C.P. Kubiak, D. Janes, R. Reifenberger, Molecular Electrostatics of Conjugated Self-Assembled Monolayers on Au(111) Using Electrostatic Force Microscopy, Langmuir. 18 (2002) 5120–5125. https://doi.org/10.1021/la0157014.

[10]   M. Castronovo, F. Bano, S. Raugei, D. Scaini, M. Dell'Angela, R. Hudej, L. Casalis, G. Scoles, Mechanical Stabilization Effect of Water on a Membrane-like System, J. Am. Chem. Soc. 129 (2007) 2636–2641. https://doi.org/10.1021/ja067462i.

[11]   B. Sanavio, D. Scaini, C. Grunwald, G. Legname, G. Scoles, L. Casalis, Oriented Immobilization of Prion Protein Demonstrated via Precise Interfacial Nanostructure Measurements, ACS Nano. 4 (2010) 6607–6616. https://doi.org/10.1021/nn101872w.

[12]   S. Chiodini, G. D'Avino, L. Muccioli, L. Bartolini, D. Gentili, S. Toffanin, C. Albonetti, Self-organization of complete organic monolayers via sequential post-deposition annealing, Prog. Org. Coatings. 138 (2020). https://doi.org/10.1016/j.porgcoat.2019.105408.

[13]   C. Albonetti, S. Chiodini, P. Annibale, P. Stoliar, R. V Martinez, R. Garcia, F. Biscarini, Quantitative phase-mode electrostatic force microscopy on silicon oxide nanostructures, J. Microsc. n/a (2020). https://doi.org/10.1111/jmi.12938.

[14]   D. Scaini, M. Castronovo, L. Casalis, G. Scoles, Electron transfer mediating properties of hydrocarbons as a function of chain length: A differential scanning conductive tip atomic force microscopy investigation, ACS Nano. 2 (2008) 507–515. https://doi.org/10.1021/nn700342p.

[15]   C. Nogues, M. Wanunu, A rapid approach to reproducible, atomically flat gold films on mica, Surf. Sci. 573 (2004) L383–L389. https://doi.org/https://doi.org/10.1016/j.susc.2004.10.019.

[16]   P. Gupta, K. Loos, A. Korniakov, C. Spagnoli, M. Cowman, A. Ulman, Facile Route to Ultraflat SAM-Protected Gold Surfaces by "Amphiphile Splitting," Angew. Chemie Int. Ed. 43 (2004) 520–523. https://doi.org/10.1002/anie.200352249.

[17]   M. Hegner, P. Wagner, G. Semenza, Ultralarge atomically flat template-stripped Au surfaces for scanning probe microscopy, Surf. Sci. 291 (1993) 39–46. https://doi.org/https://doi.org/10.1016/0039-6028(93)91474-4.

[18]   S. Xu, S. Miller, P.E. Laibinis, G. Liu, Fabrication of Nanometer Scale Patterns within Self-Assembled Monolayers by Nanografting, Langmuir. 15 (1999) 7244–7251. https://doi.org/10.1021/la9906727.

[19]   S. Ryu, G.C. Schatz, Nanografting: Modeling and Simulation, J. Am. Chem. Soc. 128 (2006) 11563–11573. https://doi.org/10.1021/ja063138b.

[20]   W.J. Price, S.A. Leigh, S.M. Hsu, T.E. Patten, G.Y. Liu, Measuring the size dependence of young's modulus using force modulation atomic force microscopy, J. Phys. Chem. A. 110 (2006) 1382–1388. https://doi.org/10.1021/jp0544540.

[21]   F. Bano, L. Fruk, B. Sanavio, M. Glettenberg, L. Casalis, C.M. Niemeyer, G. Scoles, Toward Multiprotein Nanoarrays Using Nanografting and DNA Directed Immobilization of Proteins, Nano Lett. 9 (2009) 2614–2618. https://doi.org/10.1021/nl9008869.

[22]   S.N. Magonov, V. Elings, M.-H.H. Whangbo, Phase imaging and stiffness in tapping-mode atomic force microscopy, Surf. Sci. 375 (1997) L385–L391. https://doi.org/https://doi.org/10.1016/S0039-6028(96)01591-9.

[23]   R. García, R. Pérez, Dynamic atomic force microscopy methods, Surf. Sci. Rep. 47 (2002) 197–301. https://doi.org/https://doi.org/10.1016/S0167-5729(02)00077-8.

[24]   J.E. Sader, J.W.M. Chon, P. Mulvaney, Calibration of rectangular atomic force microscope cantilevers, Rev. Sci. Instrum. 70 (1999) 3967–3969. https://doi.org/10.1063/1.1150021.

[25]   M.-H. Whangbo, G. Bar, R. Brandsch, Description of phase imaging in tapping mode atomic force microscopy by harmonic approximation, Surf. Sci. 411 (1998) L794–L801. https://doi.org/10.1016/S0039-6028(98)00349-5.

[26]   J.P. Cleveland, B. Anczykowski, A.E. Schmid, V.B. Elings, Energy dissipation in tapping-mode atomic force microscopy, Appl. Phys. Lett. 72 (1998) 2613–2615. https://doi.org/10.1063/1.121434.

[27]   G. Bar, S. Rubin, A.N. Parikh, B.I. Swanson, T.A. Zawodzinski, M.-H. Whangbo, Scanning Force Microscopy Study of Patterned Monolayers of Alkanethiols on Gold. Importance of Tip−Sample Contact Area in Interpreting Force Modulation and Friction Force Microscopy Images, Langmuir. 13 (1997) 373–377. https://doi.org/10.1021/la960935m.

[28]   F.W. Delrio, C. Jaye, D.A. Fischer, R.F. Cook, Elastic and adhesive properties of alkanethiol self-assembled monolayers on gold, Appl. Phys. Lett. 94 (2009) 2009–2011. https://doi.org/10.1063/1.3111440.

[29]   F. Purkl, A. Daus, T.S. English, J. Provine, A. Feyh, G. Urban, T.W. Kenny, Measurement of Young's modulus and residual stress of atomic layer deposited Al2O3and Pt thin films, J. Micromechanics Microengineering. 27 (2017) 85008. https://doi.org/10.1088/1361-6439/aa73e6.

[30]   M. Liu, N.A. Amro, G. Liu, Nanografting for Surface Physical Chemistry, Annu. Rev. Phys. Chem. 59 (2008) 367–386. https://doi.org/10.1146/annurev.physchem.58.032806.104542.

[31]   V.B. Engelkes, C.D. Frisbie, Simultaneous Nanoindentation and Electron Tunneling through

Alkanethiol Self-Assembled Monolayers, J. Phys. Chem. B. 110 (2006) 10011–10020. https://doi.org/10.1021/jp055567m.

[32] M.D. Porter, T.B. Bright, D.L. Allara, C.E.D. Chidsey, Spontaneously organized molecular assemblies. 4. Structural characterization of n-alkyl thiol monolayers on gold by optical ellipsometry, infrared spectroscopy, and electrochemistry, J. Am. Chem. Soc. 109 (1987) 3559–3568. https://doi.org/10.1021/ja00246a011.

[33] L. Ramin, A. Jabbarzadeh, Effect of compression on self-assembled monolayers: a molecular dynamics study, Model. Simul. Mater. Sci. Eng. 20 (2012) 85010. https://doi.org/10.1088/0965-0393/20/8/085010.

[34] S.N. Novikov, S.P. Timoshenkov, Measurements of contact potential difference (work functions) of metals and semiconductors surface by the static ionized capacitor method, Adv. Colloid Interface Sci. 105 (2003) 329–339. https://doi.org/https://doi.org/10.1016/S0001-8686(03)00051-4.

[35] H.B. Michaelson, The work function of the elements and its periodicity, J. Appl. Phys. 48 (1977) 4729–4733. https://doi.org/10.1063/1.323539.

[36] B. de Boer, A. Hadipour, M.M. Mandoc, T. van Woudenbergh, P.W.M. Blom, Tuning of Metal Work Functions with Self-Assembled Monolayers, Adv. Mater. 17 (2005) 621–625. https://doi.org/10.1002/adma.200401216.

[37] H.S. Ishii K Ito, E Seki, K, Energy level alignment and interfacial electronic structures at organic metal and organic organic interfaces, Adv. Mater. 11 (1999) +. https://doi.org/10.1002/(SICI)1521-4095(199906)11:8<605::AID-ADMA605>3.0.CO;2-Q.

[38] C. Albonetti, G. Olivieri, A. Shehu, S.D. Quiroga, M. Murgia, F. Biscarini, Unravelling molecular disorder at SAM-functionalized charge injection interfaces in organic field-effect transistors, Org. Electron. 100 (2022) 106360. https://doi.org/https://doi.org/10.1016/j.orgel.2021.106360.

[39] J. Kim, J.P. Hinestroza, W. Jasper, R.L. Barker, Application of electrostatic force microscopy on characterizing an electret fiber: Effect of tip to specimen distance on phase shift, Fibers Polym. 12 (2011) 89–94. https://doi.org/10.1007/s12221-011-0089-1.

[40] M.A. Rampi, O.J.A. Schueller, G.M. Whitesides, Alkanethiol self-assembled monolayers as the dielectric of capacitors with nanoscale thickness, Appl. Phys. Lett. 72 (1998) 1781–1783. https://doi.org/10.1063/1.121183.

[41] C. Albonetti, S. Casalini, F. Borgatti, L. Floreano, F. Biscarini, Morphological and mechanical properties of alkanethiol self-assembled monolayers investigated via bimodal atomic force microscopy, Chem. Commun. (2011). https://doi.org/10.1039/c1cc12567b.

[42] F. Schreiber, Structure and growth of self-assembling monolayers, Prog. Surf. Sci. 65 (2000) 151–257.

[43] S. Casalini, A. Shehu, S. Destri, W. Porzio, M.C. Pasini, F. Vignali, F. Borgatti, C. Albonetti, F. Leonardi, F. Biscarini, Organic field-effect transistors as new paradigm for large-area molecular junctions, Org. Electron. (2012). https://doi.org/10.1016/j.orgel.2012.01.020.

[44] P. Stoliar, R. Kshirsagar, M. Massi, P. Annibale, C. Albonetti, D.M. De Leeuw, F. Biscarini,

Charge Injection Across Self-Assembly Monolayers in Organic Field-Effect Transistors : Odd - Even Effects, J. Am. Chem. Soc. (2007) 1060–1064. https://doi.org/10.1021/JA069235M.

[45] G. Ashkenasy, D. Cahen, R. Cohen, A. Shanzer, A. Vilan, Molecular Engineering of Semiconductor Surfaces and Devices, Acc. Chem. Res. 35 (2002) 121–128. https://doi.org/10.1021/ar990047t.

[46] L. Belding, S.E. Root, Y. Li, J. Park, M. Baghbanzadeh, E. Rojas, P.F. Pieters, H.J. Yoon, G.M. Whitesides, Conformation, and Charge Tunneling through Molecules in SAMs, J. Am. Chem. Soc. 143 (2021) 3481–3493. https://doi.org/10.1021/jacs.0c12571.

[47] N. Nishi, D. Hobara, M. Yamamoto, T. Kakiuchi, Chain-length-dependent change in the structure of self-assembled monolayers of n-alkanethiols on Au(111) probed by broad-bandwidth sum frequency generation spectroscopy, J. Chem. Phys. 118 (2003) 1904–1911. https://doi.org/10.1063/1.1531098.

[48] L.H. Li, T. Tian, Q. Cai, C.-J. Shih, E.J.G. Santos, Asymmetric electric field screening in van der Waals heterostructures, Nat. Commun. 9 (2018) 1271. https://doi.org/10.1038/s41467-018-03592-3.

[49] F. Biscarini, Q.K. Ong, C. Albonetti, F. Liscio, M. Longobardi, K.S. Mali, A. Ciesielski, J. Reguera, C. Renner, S. De Feyter, P. Samorì, F. Stellacci, Quantitative analysis of scanning tunneling microscopy images of mixed-ligand-functionalized nanoparticles, Langmuir. 29 (2013). https://doi.org/10.1021/la403546c.

[50] D. Nečas, P. Klapetek, Gwyddion: an open-source software for SPM data analysis, Cent. Eur. J. Phys. 10 (2012) 181–188. https://doi.org/10.2478/s11534-011-0096-2.
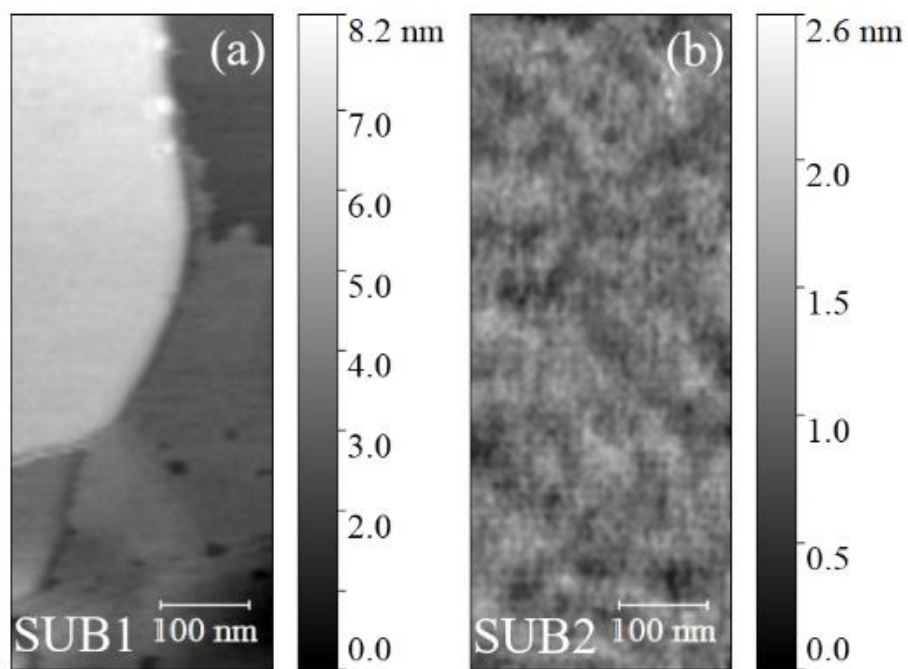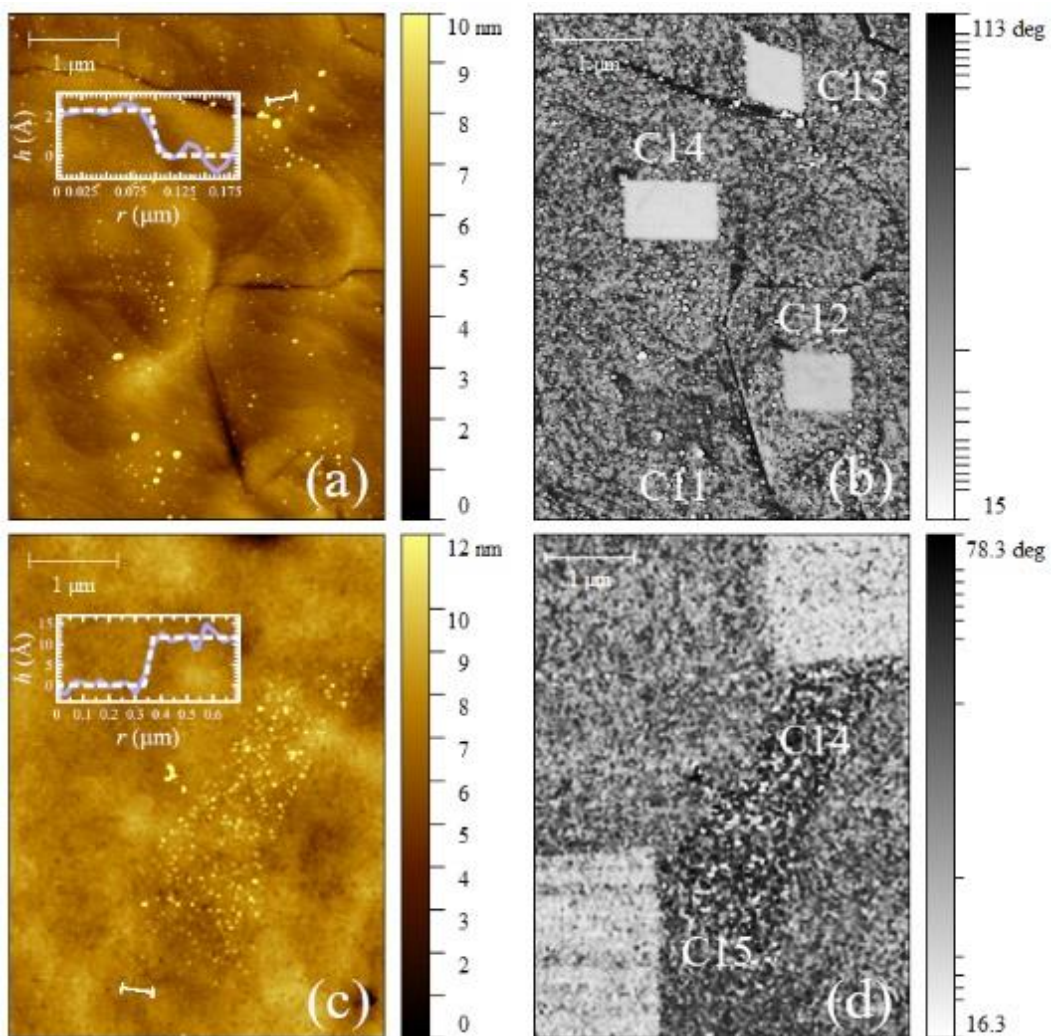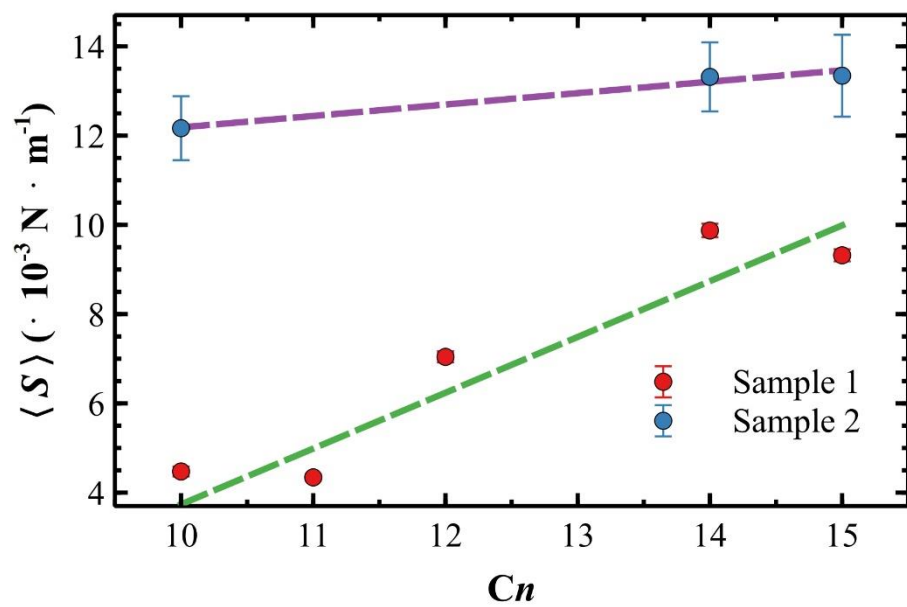
Figure 1

Figure 2

Figure 3

Figure 4

Sample1

Sample2

Figure 5

Sample1   Sample2

Figure 6

Sample1
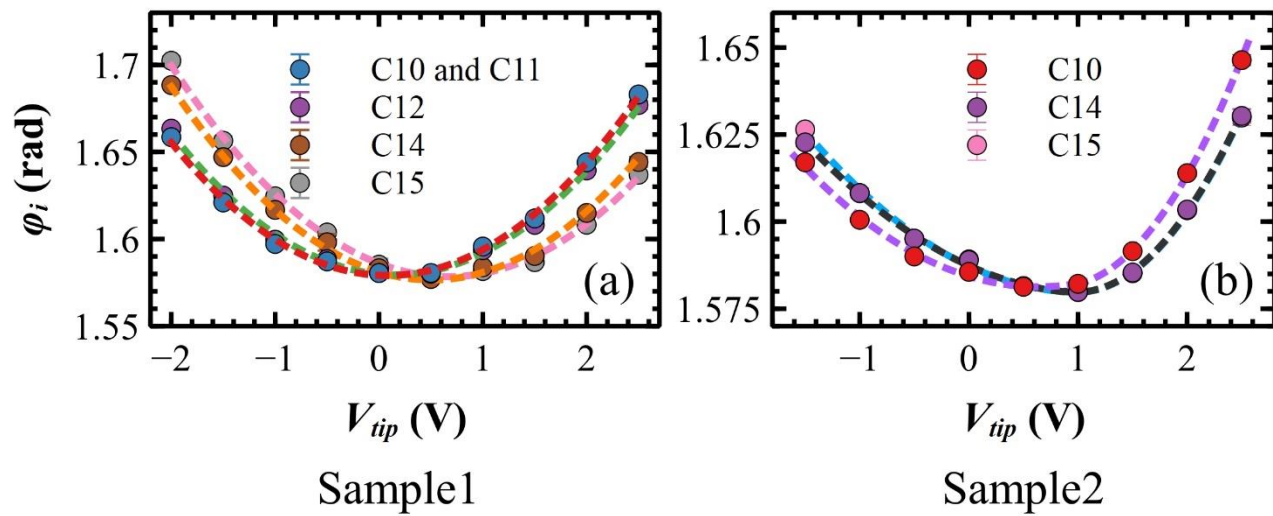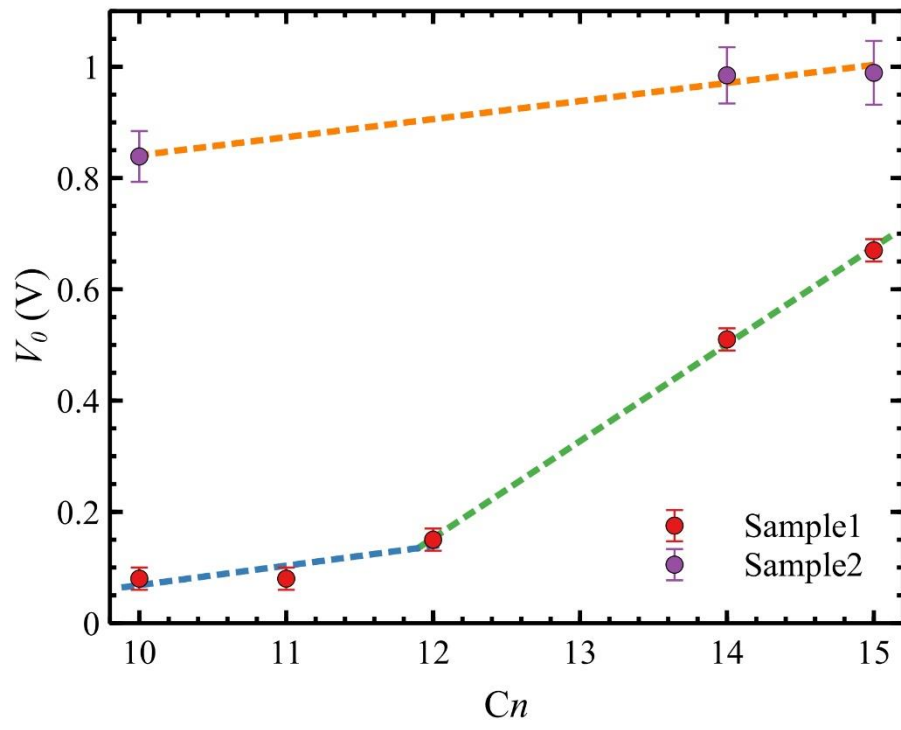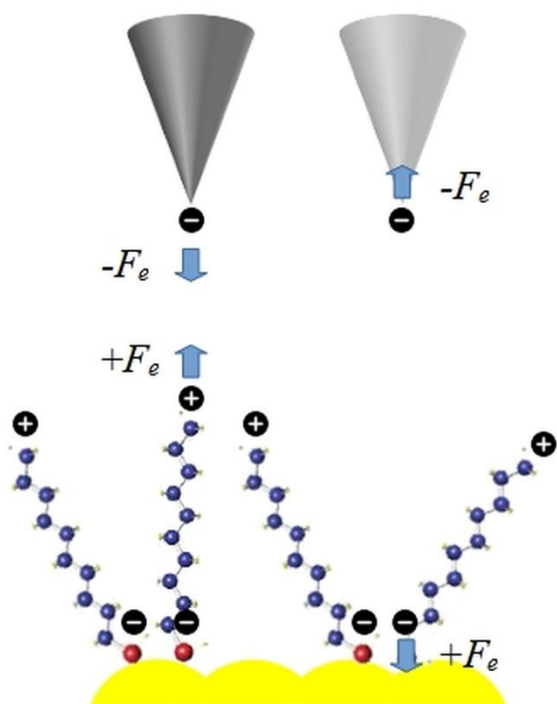
Sample2
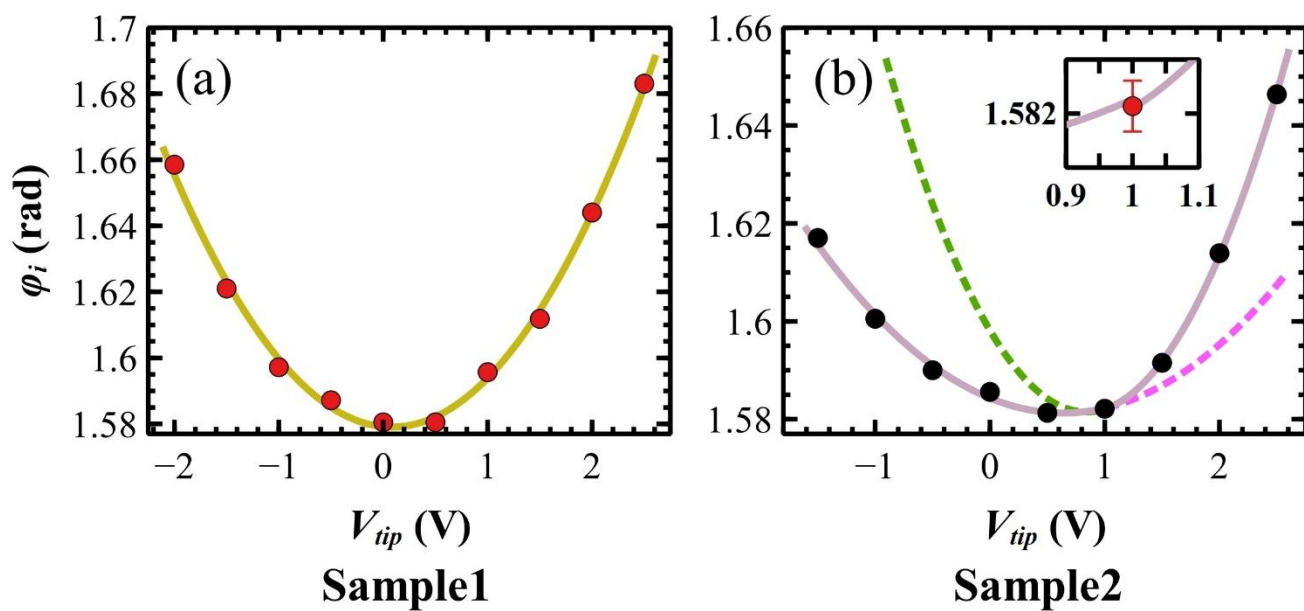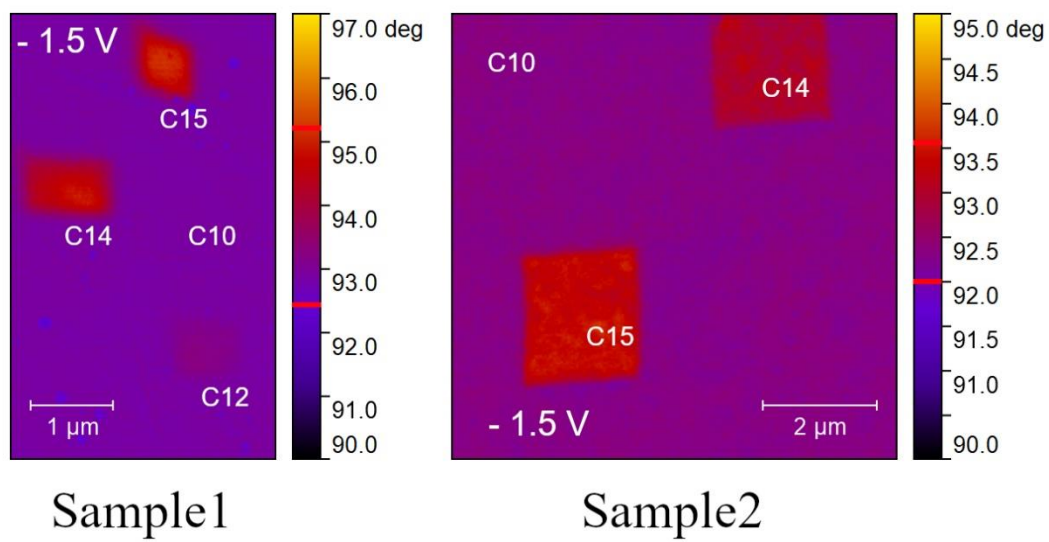
Figure 7

Figure 8

Captions

Figure 1: Topographic images of the two different template-stripped Au substrates: flame annealed SUB1 (a), and not annealed SUB2 (b). Substrates topographies were obtained in two consecutive steps: firstly, the SAM is removed by nanoshaving [18], and then the exposed substrate surface is imaged by contact mode with the same tip used for shaving the SAM. The size of the images is $\approx 300 \times 750$ nm^2, comparable with the dimension of the nanografted patches.

Figure 2: Topographic (a, c) and phase (b, d) images of the nanografted samples (Sample1: a, b; Sample2: c, d). The alkanethiol patches present small height changes in the topographic images. The inset plots in Figure (a) and (c) show the topographic cross-section profiles of the two C15 patches (see white line profiles with end markers in topographic images – additional line profiles are reported in the Supplementary Materials). The features of the Au substrates are clearly visible due to the different methods adopted for their preparation (cp. to Experimental and Method sections). To boost the phase contrast, a Gray-inverted color bar and an adaptive non-linear color mapping is used [50], especially in order to distinguish the C10 and C11 patches in Figure (a). The ICM measurements are performed by using silicon cantilevers with (a) resonant frequency $\omega_0 \approx 131$ kHz, cantilever quality factor $Q \approx 178$, and $k \approx 1.89$ N·m^{-1}; and (b) $\omega_0 \approx 128$ kHz, $Q \approx 237$ and $k \approx 2.44$ N·m^{-1}

Figure 3: Average stiffness $\langle S \rangle$ versus alkanethiol length Cn, where n stands for the alkane chain length ranging from 10 to 15, and correspondent regression fitting lines for Sample1 (red dots) and Sample2 (blue dots).

Figure 4: Phase curves φ_i versus V_{tip} obtained on the C10 SAM matrix for Sample1 (a) and Sample2 (b). The fitting is performed with a parabola for Sample1 (sand color solid line) or a combination of two parabolas (green and pink dashed lines) to perform a better data fitting (purple solid line).

Figure 5: EFM-phase images of Sample1 (left) and Sample2 (right) for $V_{tip} = -1.5$ V. The false color bar for the phase values reports the raw data recorded by the microscope, i.e. in degree.

Figure 6: Phase curves φ_i versus V_{tip} obtained on the C10 SAM matrix for Sample1 (a) and Sample2 (b). The fitting is performed with a parabola for Sample1 (sand color solid line) or a linear combination of two parabolas (green and pink dashed lines) to perform a better data fitting (purple solid line).

Figure 7: Progress of the CPD V_0 for increasing alkane chain length Cn. Two portions with a linear fitting can be observed for Sample1, while only one for Sample2 that has a slope comparable to the lower one of Sample1 (dashed lines).

Figure 8: Sketch of the electrostatic forces (F_e) acting between the EFM tip (negatively biased) and a disordered alkanethiol SAM on a rougher Au layer (the disorder is intentionally amplified for graphical purposes). The positive charges at the SAM/air interface determine an attractive force on the tip, that becomes repulsive when the tip is exposed to the negative charges at the Au/SAM interface.